Available online at www.sciencedirect.com
ScienceDirect
Trans. Nonferrous Met. Soc. China 26(2016) 2263−2275
Transactions of Nonferrous Metals Society of China
www.tnmsc.cn

Effect of aging time on precipitation behavior, mechanical and corrosion properties of a novel Al−Zn−Mg−Sc−Zr alloy

Bo LI[1], Qing-lin PAN[2], Cong-ping CHEN[1], Zhi-min YIN[2]

1. College of Mechanical and Power Engineering, China Three Gorges University, Yichang 443002, China;
2. School of Materials Science and Engineering, Central South University, Changsha 410083, China

Received 7 September 2015; accepted 11 January 2016

Abstract: The precipitation behavior, mechanical properties and corrosion resistance of a novel Al−Zn−Mg−Sc−Zr alloy aged at different time were studied by optical microscopy (OM), scanning electron microscopy (SEM), transmission electron microscopy (TEM), tensile tests, potentiodynamic polarization and electrochemical impedance spectroscopy. The results revealed that with increasing aging time at 120 °C, the hardness and tensile strength of the alloy increased rapidly at first and then slightly decreased. The resistance of exfoliation corrosion (EXCO) and intergranular corrosion (IGC) increased gradually with increasing aging time. The same trend of corrosion properties was demonstrated by electrochemical polarization curves and EIS test. The characteristics of grain boundary precipitates and precipitate free zone (PFZ) had a significant influence on the mechanical and corrosion behaviors of the studied alloy. On the basis of TEM observations, the size of grain boundary precipitates and the width of PFZ became larger, and the distributed spacing of grain boundary precipitates was enhanced with increasing aging time.

Key words: aluminum alloy; heat treatment; precipitation behavior; $Al_3(Sc, Zr)$ particles; electrochemical impedance spectroscopy

1 Introduction

As a typical age-hardenable alloy, Al−Zn−Mg alloys have been attracting a great research interest regarding structural applications in aerospace and aeronautic field due to high specific strength and good mechanical properties [1−3]. In order to well meet the requirement of aerospace and aeronautic industries, many material scientists paid more attention to improve mechanical properties [4,5]. ZHANG et al [6] investigated the microstructure and mechanical properties of Al−0.30Zr, Al−0.30Zr−0.08Y and Al−0.30Zr−0.16Y (mass fraction, %) alloys. They found that minor addition of Y refines grain size and forms eutectic Al_3Y phase particles within grains and at grain boundaries in as-cast Al−Zr−Y alloys. The mechanical properties of Al−Zr alloys get improved with increasing Y content. WU et al [7] researched the effect of Er additions on the precipitation strengthening of Al−Hf alloys. It has been found that the combined addition of 0.045% Er and 0.18% Hf (mole fraction) in Al gives a maximum hardness of 640 MPa, which is significantly higher than that of the Al−0.18Hf and Al−0.045Er alloys. The remarkable strengthening can be attributed to the addition of Er, which accelerates the precipitation kinetics and stimulates the decomposition of Al−Hf. VO et al [8] studied nanosized precipitates in an Al−0.06Sc (mole fraction, %) alloy containing various microalloying additions (Si, Zr and Er). The results showed that substituting 0.005% Er (mole fraction) for the more expensive Sc maintains high ambient-temperature strength, and dramatically improves the high-temperature creep resistance, as anticipated from the increase in lattice parameter mismatch between the α(Al) (FCC) matrix and the coherent $L1_2$-ordered Al_3(Sc,Zr,Er) precipitates. DENG et al [9] investigated the effects of Sc and Zr microalloying additions on the recrystallization texture and mechanism of Al−Zn−Mg alloys during annealing. However, under a humid environment, Al−Zn−Mg alloys are sensitive to localized corrosion, such as exfoliation corrosion (EXCO) and intergranular corrosion (IGC). Adding minor rare earth elements to Al−Zn−Mg alloys cannot completely improve poor corrosion resistance. Therefore, it is vital

Foundation item: Project (2012CB619503) supported by the National Basic Research Program of China; Projects (51475266, 51005134) supported by the National Natural Science Foundation of China
Corresponding author: Bo LI; Tel/Fax: +86-717-6397560; E-mail: liboctgu@163.com
DOI: 10.1016/S1003-6326(16)64347-9

to find an effective way to not only improve corrosion resistance but also enhance mechanical properties.

As is well known, the corrosion resistance of metal and alloys can also be improved by heat-treatment process [10−12]. Meanwhile, Al−Zn−Mg alloys are sensitive to corrosion cracking in sodium chloride solution and often exhibit different forms of corrosion, such as EXCO, IGC and stress corrosion cracking (SCC), due to damp air and industrial waste gas. Therefore, investigating their exfoliation corrosion properties would be very important to their application. WANG et al [13] investigated microstructural evolution, corrosion resistance and mechanical properties of an as-forged Mg−6.7%Zn−1.3%Y−0.6%Zr alloy before and after solid solution treatment (T4). The results revealed that the proposed T4 treatment can improve corrosion resistance of the alloy. ROGAL et al [14] researched mechanical properties and corrosion resistance of steel X210CrW12 after semi-solid processing and heat treatment. LI et al [15] studied the effects of age-forming on microstructure, mechanical and corrosion properties of a novel Al−Li alloy. They found that age-forming in the novel Al−Li alloy enhances the mechanical properties, meanwhile, improves the corrosion resistance. WANG et al [16] developed a new two-step aging treatment to improve intergranular corrosion (IGC) resistance of Al−Mg−Si−Cu alloys without strength loss compared with that of the T6 temper.

Unfortunately, few reports have systemataically investigated the effects of aging heat treatment on precipitation behavior, mechanical and corrosion properties of Al−Zn−Mg alloy with minor Sc and Zr elements. The objective of this work was to explore the effect of aging heat treatment on exfoliation corrosion and intergranular corrosion behaviors of the studied alloy. Meanwhile, microstructure evolution and mechanical properties of the studied alloy were also researched.

2 Experimental

The experimental alloy with chemical composition of Al−5.45Zn−1.96Mg−0.37Cu−0.28Mn−0.26Sc−0.11Zr (mass fraction, %) was prepared with pure Al, pure Mg, pure Zn and Al−Sc, Al−Zr, Al−Cu, Al−Mn master alloys by ingot metallurgy in a crucible furnace. The ingot was homogenized at 470 °C for 24 h, hot-rolled to 7 mm and then cold-rolled to 2 mm thin plates. These specimens were solid solution treated at 470 °C for 1 h, subsequently water-quenched and then immediately aged at 120 °C for 4, 12, 24, 32 and 48 h, respectively.

The tensile tests were conducted on an MTS810 tester, on flaky samples with 2 mm in thickness and 28 mm in gauge length. Vickers hardness tests were carried out on a 401MVDTM digital Vickers microhardness analyzer at duration time of 15 s. The EXCO test was performed as described in GB/T 22639−2008 [17]. The IGC tests were performed according to GB/T 7998−2005 [18]. Electrochemical measurement was carried out with three-electrode system. EIS tests were carried out at the open circuit potential. The microstructure characterization and the depths of attack were measured under optical microscopy. Electrochemical measurement was carried out with a three-electrode system. Electrochemical impedance spectroscopy (EIS) tests were carried out at the open circuit potential.

The microstructure observation of the studied alloy was illustrated by OM, SEM and TEM. POLYVER-MET metallographic microscope was employed for metallographic microstructure analyses. SEM observations were carried out on a Quanta MK2−200 SEM, operating at 20 kV. TEM specimens were prepared by twin jet electro-polishing in a 30% nitric acid and 70% ethanol solution at −30 °C, and observed on a TECNAIG^2 20 electron microscope.

3 Results and discussion

3.1 Microstructure evolution

Figure 1 presents SEM images of the as-cast alloys. It can be easily found that the studied alloy ingot exhibits serious segregation phenomenon. In addition, large amounts of intermetallic phases at the grain boundaries can also be observed. On the basis of EDS analyses, Points *A* and *B* of Fig. 1(b) present the white secondary phases, which contain a large number of Zn and Mg elements. It may be the mixture of supersaturated solid solution α(Al), η-$MgZn_2$ and T-$Mg_{32}(Al,Zn)_{49}$. The grey phases as shown in Points *C* and *D* of Fig. 1(b) were the impurity phase, which might be α(Al) matrix with solute of Zn, Mg, Fe and Si elements. Table 1 presents the EDS results. In addition, massive intermediate compounds can seriously affect the subsequent processing properties of the studied alloy [19−21]. Therefore, it is necessary to eliminate severe segregation by homogenization treatment.

OM and SEM images of the homogenized studied

Table 1 Chemical compositions of secondary phases

Point in Fig. 2(b)	Mole fraction/%						
	Al	Zn	Mg	Cu	Mn	Fe	Si
A	68.25	15.93	13.24	2.58	0	0	0
B	70.15	12.54	14.21	3.10	0	0	0
C	82.65	2.33	2.19	1.23	2.15	6.58	2.87
D	79.86	1.81	2.66	1.91	2.48	8.24	3.04

alloys are shown in Fig. 2. After homogenization treatment (470 °C, 24 h), serious segregation is almost eliminated, dissoluble Zn and Mg enriched non-equilibrium phases along grain boundaries dissolve into α(Al) matrix completely. But there are still little indissoluble impurity phases containing Fe and Si elements both in the grains and along the grain boundaries. Figure 3(a) presents TEM image of the homogenized alloy. From Fig. 3(a), a great number of nanometer-sized particles like a hoof are distributed within α(Al) matrix. The SAED pattern of the studied alloy in $[011]_{Al}$ projection is shown in Fig. 3(b). The diffraction spot from α(Al) matrix has been indexed, these spots are coherent $Al_3(Sc, Zr)$ particles with an Ll_2 cubic crystal structure. It is well known that the $Al_3(Sc,Zr)$ particles have a good thermal stability and drastic antirecrystallized effect, which can strongly pin dislocation and effectively prevent recrystallization [22].

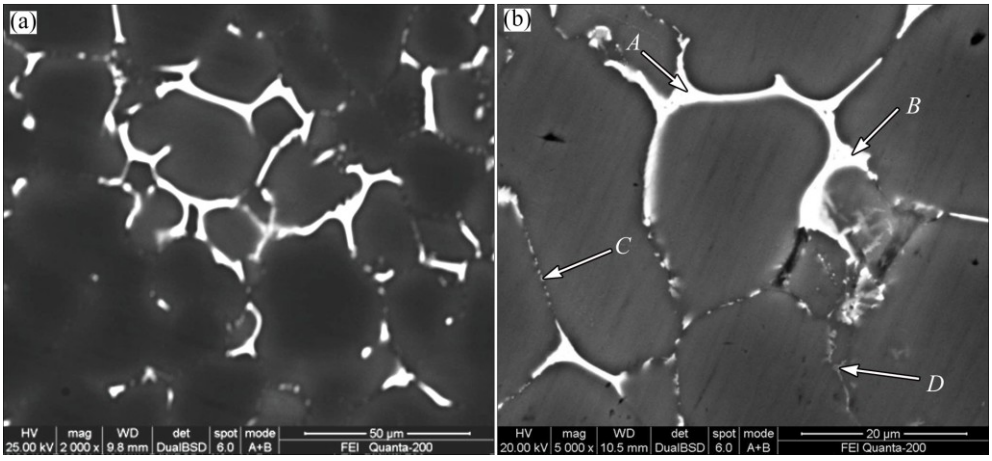

Fig. 1 SEM images of as-cast alloys: (a) Low magnification; (b) High magnification

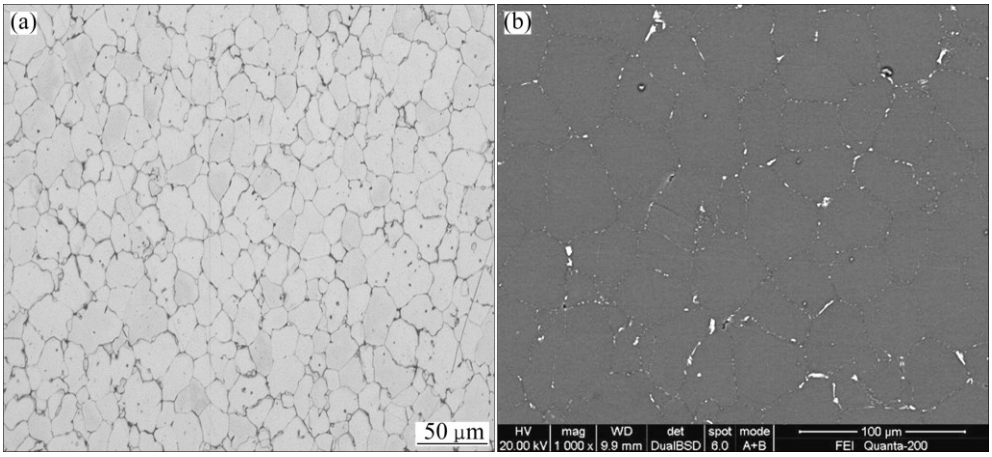

Fig. 2 Microstructures of homogenized alloy: (a) OM image; (b) SEM image

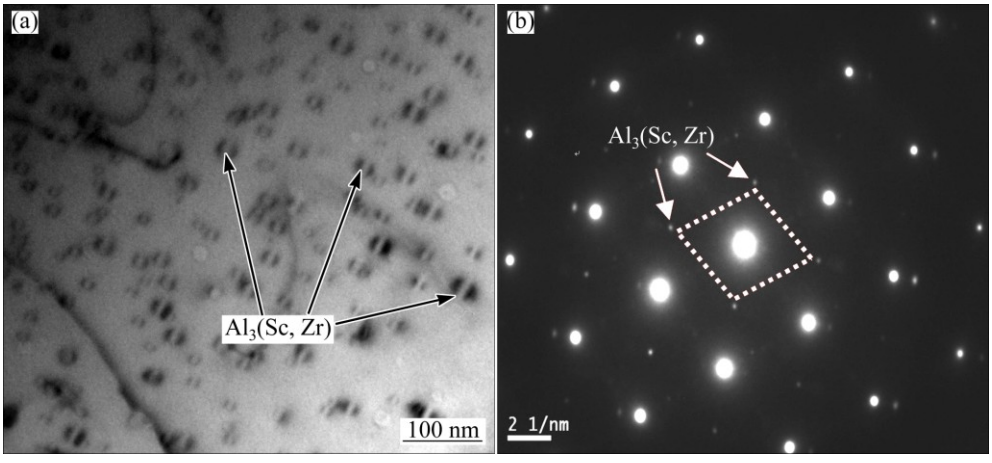

Fig. 3 TEM image and SAD pattern of alloy: (a) Homogenized at 470 °C for 24 h; (b) SAED pattern in $[001]_{Al}$ projection

Figure 4 shows the line scanning traces of as-cast and homogenized alloys. As shown in Fig. 4(a), Zn, Mg and Cu elements distribute unevenly from grain boundary to the inside of the alloy. After homogenization treatment at 470 °C for 24 h, it can be found from Fig. 4(b) that the segregation of the main elements Zn, Mg and Cu is almost eliminated, and the elements distribution is homogeneous from grain boundary to the inside of the studied alloy.

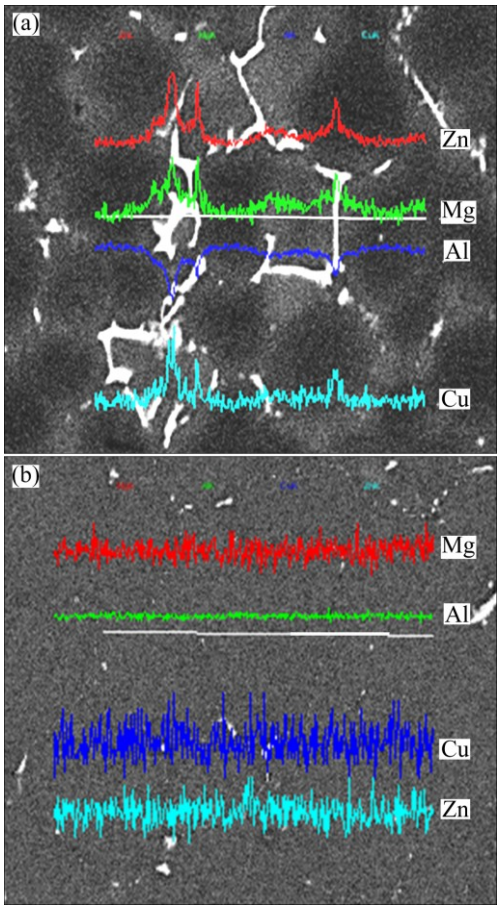

Fig. 4 Line scanning analysis of studied alloy: (a) As-cast; (b) Homogenized at 470 °C for 24 h

The SEM images of the studied alloy under different conditions are shown in Fig. 5. The grains structures of the studied alloy are elongated, which present typical fibrous structure along rolling direction after being hot-rolled (Fig. 5(a)). As shown in Fig. 5(b), the fibrous structure of the studied alloy becomes finer. In addition, there exist massive non-equilibrium phases during rolling process. After solution treatment at 470 °C for 1 h (Fig. 5(c)), the non-equilibrium phases are dissolved into α(Al) matrix, only a few of impurity phases can be found in the studied alloy [23−25].

The microstructures of aged alloys were observed by TEM. The TEM images of the studied alloy after aging at 120 °C for different time are shown in Fig. 6. For aging at 4 and 12 h, it can be easily found that the

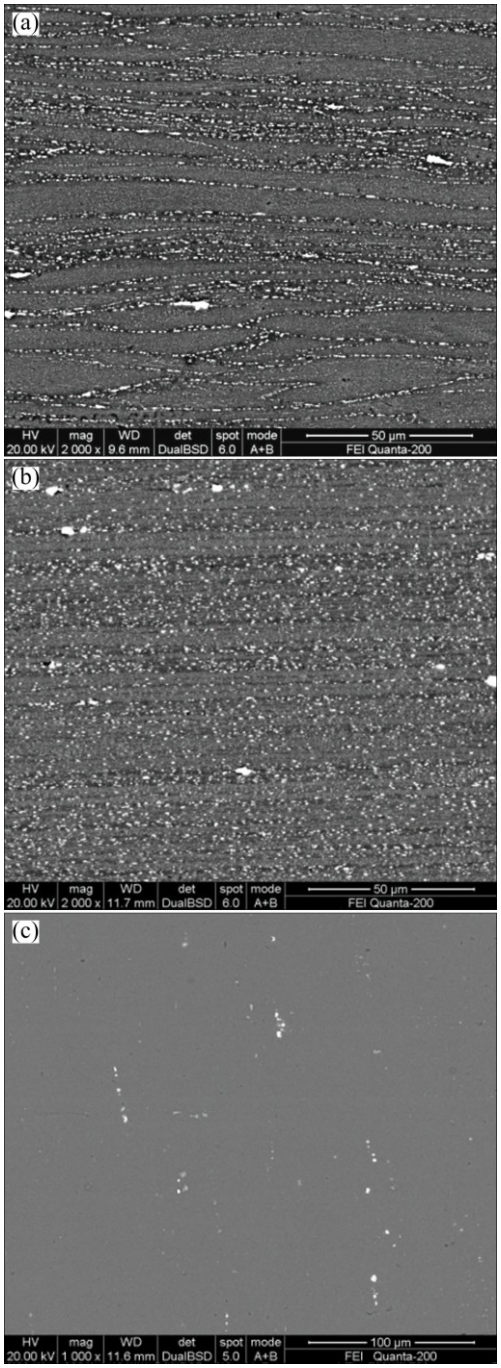

Fig. 5 SEM images of studied alloys: (a) Hot-rolled; (b) Cold-rolled; (c) Solution treated at 470 °C for 1 h

ultrafine η' precipitates with high density are distributed within α(Al) matrix, and the precipitates along grain boundaries are continuous and the sizes are small, as shown in Figs. 6(a) and (b). After aging at 120 °C for 24 h (Fig. 6(c)), a mass of dispersively distributed η' precipitates grow and aggregate during aging process. As shown in Fig. 6(d), after aging at 120 °C for 32 h, distinctly coarse and discrete grain-boundary precipitates (η) are formed. Meanwhile, PFZ is formed. More precipitates transform from metastable η' precipitates to stable η precipitates. The η precipitates are coarsening

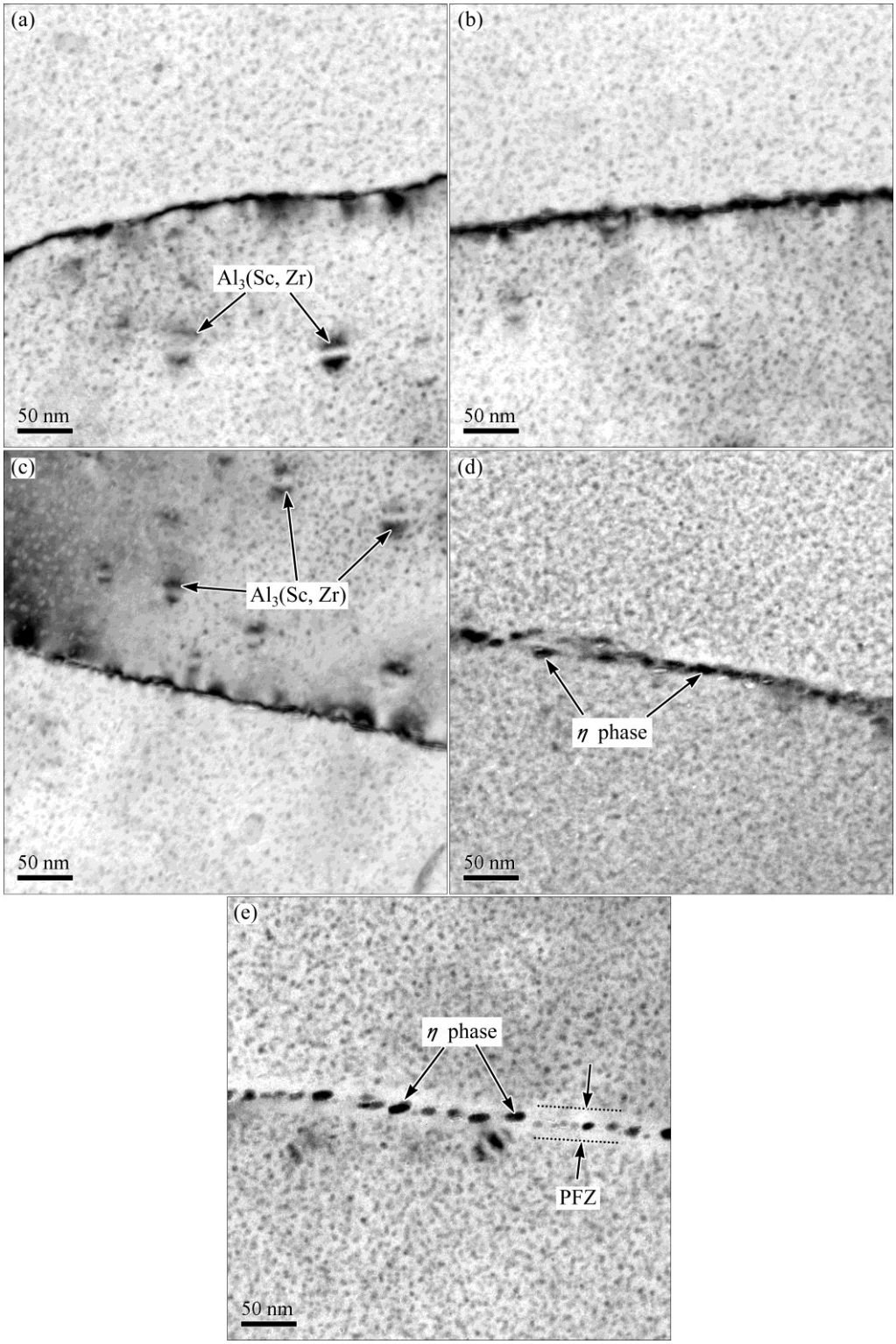

Fig. 6 TEM images of studied alloy after aged at 120 °C for various time: (a) 4 h; (b) 12 h; (c) 24 h; (d) 32 h; (e) 48 h

and completely discontinuous along grain boundary (Fig. 6(d)). With increasing aging time (Fig. 6(e)), the distributed spacing and grain size of grain boundary precipitates are mostly larger. The PFZ with 35−40 nm in width can be easily observed along grain boundary. In addition, there also exist lots of fine Al_3(Sc,Zr) particles during aging process(Figs. 6(a), (c) and (d)).

3.2 Mechanical properties

Figure 7(a) presents the tensile properties of the alloy at different aging time. It can be found that both the ultimate tensile strength and yield strength values increase first and then decrease with increasing aging time. Compared with the ultimate tensile strength (UTS) and yield strength (YS) values, the elongation (El) of the

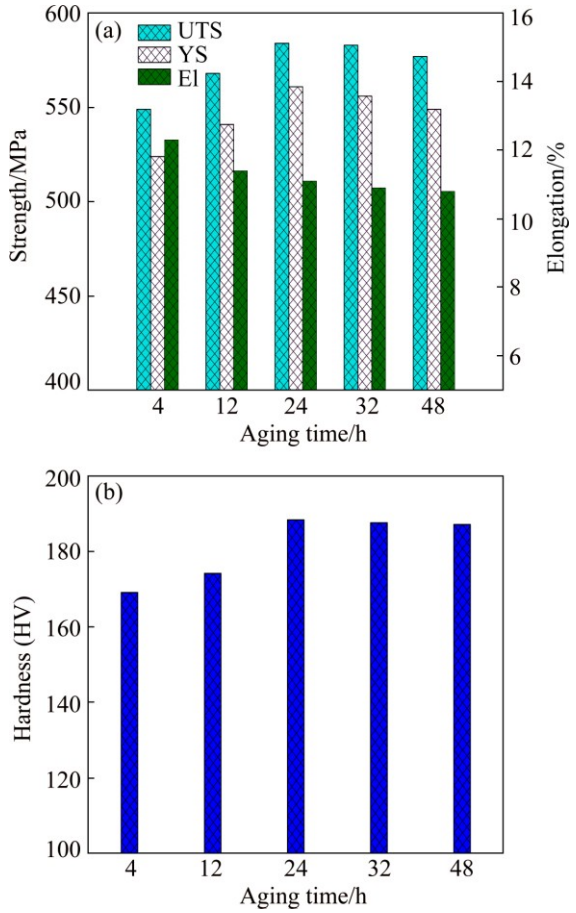

Fig. 7 Mechanical properties of alloy aged at 120 °C for various time

alloy has the opposite trend. When aging at 120 °C for 4, 12 and 24 h, the ultimate tensile strength and yield strength of the studied alloy increase with increasing aging time. The tensile strength of the studied alloy can reach a maximum value at 120 °C for 24 h; the ultimate tensile strength, yield strength and elongation of the studied alloy can reach 584 MPa, 561 MPa and 11.2%, respectively. When aging time continues to increase to 32 h, the ultimate tensile strength and yield strength of the studied alloy begin to decrease slightly. After aging treatment at 120 °C for 48 h, the ultimate tensile strength and the yield strength decrease by 8 and 16 MPa, respectively.

The hardness of the studied alloys at various aging time is shown in Fig. 7(b). The studied alloy exhibits obvious age hardening behavior. The studied alloy hardness rapidly increases during the initial stage of aging processing. After aging treatment at 120 °C for 24 h, the hardness reaches a maximum value. With increasing aging time, the hardness of the studied alloy stays gentle for a relatively long time and then decreases gradually. The hardness of the studied alloy aged at 120 °C for 24 h is about HV 188.4, much higher than that of the alloy aged at 120 °C for 48 h. This trend is in accordance with Fig. 7(a).

As is well known, the main precipitation sequence of Al−Zn−Mg alloy can be summarized as follows: supersaturated solid solution (SSS)→GP zones→metastable $\eta'(MgZn_2)$→stable η $(MgZn_2)$ [26,27]. GP zones are formed at the initial stage of aging heat treatment. GP zones are atom clustering zones, which are coherent with α(Al) matrix. With increasing aging time, the precipitates gradually transform from GP zones to η' phase, and then η phase. The metastable hexagonal η' phase is semi-coherent with α(Al) matrix. The equilibrium η phase is non-coherent with α(Al) matrix. In these three types of precipitates, the GP zones and metastable $\eta'(MgZn_2)$ are the main aging-hardening precipitates in Al−Zn−Mg alloys. The size, distribution of GP zone and η' precipitates have a significant influence on the strength of Al−Zn−Mg alloy [28,29]. As shown in Figs. 6(a) and (b), when the studied alloy is aged at 120 °C for 4 and 12 h, the main strengthening precipitates are coherent GP zones. With increasing aging time (aging at 120 °C for 24 h), the precipitates inside the grains are homogenously distributed semi-coherent η' phases (Fig. 6(c)). After aging at 120 °C for 48 h, the η' precipitates are coarsened gradually; the distribution of η precipitates is discontinuous at grain boundary (Fig. 6(e)). However, the resistance effect of non-coherent η phases on dislocation movement is decreased; the non-coherent η phases do not contribute strongly to the strengthening effect of the studied alloy. Thus, the strength and hardness of the studied alloy aged at 120 °C for 48 h decrease.

3.3 Corrosion behavior

3.3.1 EXCO test

The exfoliation ratings for the studied alloy in the EXCO test are shown in Table 2. For the classification, N represents no appreciable attack, PA−PC indicates pitting corrosion and EA−ED describes a range from superficial to severe exfoliation. On the basis of this ranking, the

Table 2 Evolution of EXCO rating of alloy aged at 120 °C for various time

Immersion time/h	Exfoliation rating			
	120 °C, 4 h	120 °C, 12 h	120 °C, 24 h	120 °C, 48 h
2	PB	N	N	N
4	EA	PB	PA	N
6	EB	PC	PA	PA
8	EB	PC	PB	PA
12	EC	PC	PC	PB
24	EC	EB	EA	PC
36	ED	EC	EA	EA

severity of attack from high to low is (120 °C, 4 h), (120 °C, 12 h), (120 °C, 24 h), (120 °C, 32 h), (120 °C, 48 h).

In order to further research EXCO behavior of the studied alloy, the surface images of specimens were taken by digital camera. Figure 8 shows EXCO morphologies of the studied alloy at various aging time. For aging for 4 h, most of the lifted surface layers on the alloy are peeled off and raised to the upside of the solution with gas blisters caused by electrochemical reaction during exfoliation process. This is a process of the attack advancing through grain boundaries, growing parallel to the metal surface [30]. When increasing aging time, the pitting corrosion, blistering, or delamination generated during EXCO experiment have been reduced apparently (Figs. 8(b) and (c)). After aging at 120 °C for 32 h, a small amount of bubbling and etch pits appeared on the surface of the studied alloy, as presented in Fig. 8(d). Thus, the EXCO resistance of the studied alloy can be effectively improved by increasing aging time.

3.3.2 Intergranular corrosion behavior

Figure 9 illustrates the IGC morphologies of cross section of the studied alloys after immersing in ICG solution for 6 h. Table 3 shows variation range of the corrosion depths of the studied alloy. The maximum IGC depth of the studied alloy is 92 mm after aging at 120 °C for 4 h. With increasing aging time, the maximum IGC depth of the studied alloy decreases. After aging for 24 h, the maximum value of corrosion depth decreases to 58 mm. These results are in accordance with their surface appearance. Thus, the maximum IGC depths of the studied alloy can remarkably be decreased by increasing aging time. This indicates that increasing aging time can enhance IGC resistance of the studied alloy. It is well known that IGC of aluminum alloys is the result of microgalvanic cell action at the grain boundary [31]. In addition, coarsening of the grain boundary precipitates is possibly an important factor in reducing IGC susceptibility, especially if the presence of a continuous active or noble grain boundary film can be postulated [32].

In general, the corrosion resistance of aluminum alloy is mainly determined by the distribution of grain boundary precipitates, the difference in potential between PFZ, α(Al) matrix and grain boundary precipitates [33−35]. According to previous research work [10], the function mechanisms on the localized corrosion of aluminum alloy can be summarized as follows. At first, IGC is related to the distribution of grain boundary precipitates and PFZ. Grain boundaries with continuous η precipitates become the susceptive anode channel, and the continuous grain boundary precipitates offer a path for IGC. Secondly, different potentials between grain boundary precipitates, PFZ and α(Al) matrix can lead to anodic dissolution.

In order to investigate different corrosion susceptibilities of the studied alloy, it is vital to consider electrochemical behavior [36]. The corrosion potentials (φ_{corr}) for the grain boundary precipitates, PFZ and α(Al) matrix are −0.86, −0.57 and −0.68 V, respectively. The φ_{corr} values of PFZ and α(Al) matrix are positive with respect to that of the grain boundary precipitates; the

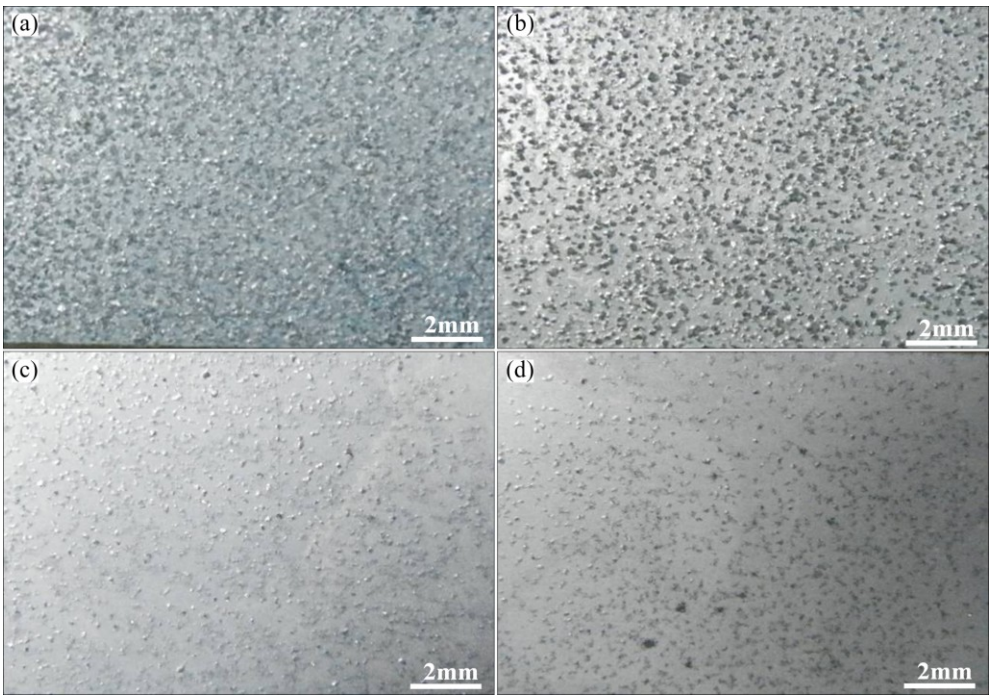

Fig. 8 Corrosion morphologies of alloy aged at 120 °C for various time after 6 h of immersion in EXCO solution: (a) 4 h; (b) 12 h; (c) 24 h; (d) 32 h

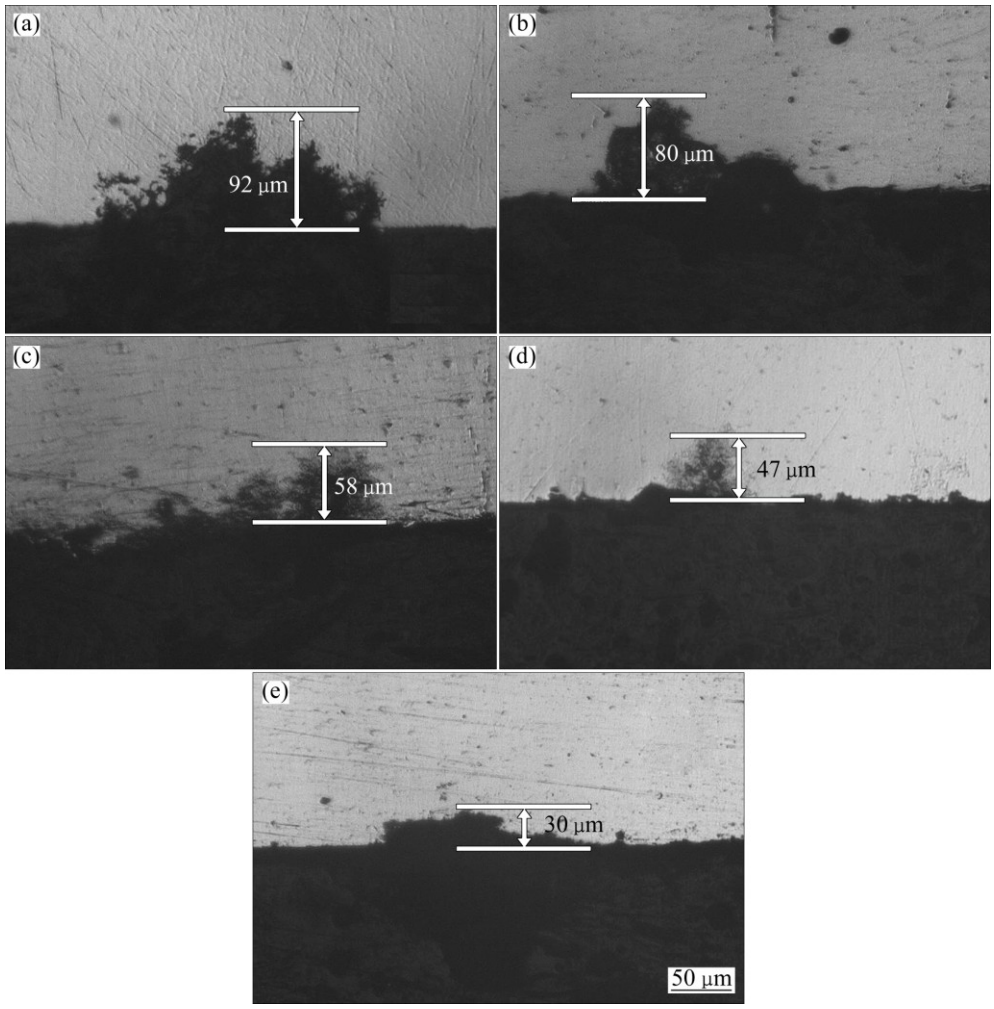

Fig. 9 IGC morphologies of cross-sections of studied alloy after aged at 120 °C for various time: (a) 4 h; (b) 12 h; (c) 24 h; (d) 32 h; (e) 48 h

Table 3 Variation range of corrosion depths of studied alloy

Aging treatment	Maximum corrosion depth/μm	Average corrosion depth/μm
120 °C, 4 h	92	77
120 °C, 12 h	80	68
120 °C, 24 h	58	49
120 °C, 32 h	47	36
120 °C, 48 h	30	23

grain boundary precipitates act as the anode to α(Al) matrix and PFZ at its periphery, leading to the anodic dissolution, and then IGC and EXCO take place. Meanwhile, EXCO is developed from IGC. The corrosion products accumulate along the grain boundaries during IGC process.

As shown in Fig. 6, after the alloy is aged at 120 °C for 4 and 12 h, the grain boundary precipitates are distributed continuously, and the continuous grain boundary precipitates can offer an active corrosion path as a result of the galvanic reaction between grain boundary precipitates and α(Al) matrix. Therefore, the corrosion susceptibility of the studied alloy is high. With increasing aging time, the grain boundary precipitates become coarser, which are distributed along grain boundaries discontinuously. The distributed spacing of grain boundary precipitates also becomes larger, and the width of the PFZ becomes larger (Figs. 6(d) and (e)). Thus, the active corrosion paths resulting from the galvanic reaction between the anodic grain boundary precipitates and the matrix at their adjacent periphery are weakened for IGC and EXCO, leading to the decrease of corrosion current density and increase of corrosion resistance. As a result, the susceptibility to IGC and EXCO decreases.

3.3.3 Analysis of polarization curves

Figure 10 represents the polarization curves of the studied alloy aged for different time in the 3.5% NaCl (mass fraction) solution. The corrosion potential (φ_{corr}), corrosion current density (J_{corr}) and polarization resistance (R_p) derived from the polarization curves, are summarized in Table 4. It is evident that aging time has

an obvious impact on the electrochemical response. As is well known, the corrosion degree is related with corrosion rate, the electrochemical corrosion rate increases linearly with decreasing the corrosion current density J_{corr} according to Faraday's law because the high corrosion speeds of anodic and cathodic kinetics result in high corrosion current density [37]. It is understandable that high rates of anodic and cathodic kinetics result in high corrosion current density [38]. As shown in Table 4, the corrosion current density (J_{corr}) of sample aged for 4 h is much higher than those of samples aged for 12, 24, 32 and 48 h, while the polarization resistance (R_p) of sample aged for 4 h is the lowest. These indicate that the alloy aged for 4 h is the most susceptible to corrosion, implying the higher corrosion efficiency. Thus, the corrosion susceptibility of the studied alloy can be ranked in the order from high to low as follows: (120 °C, 4 h), (120 °C, 12 h), (120 °C, 24 h), (120 °C, 32 h), (120 °C, 48 h). In general, it can be seen that the polarization results are in agreement with EXCO and IGC measurements.

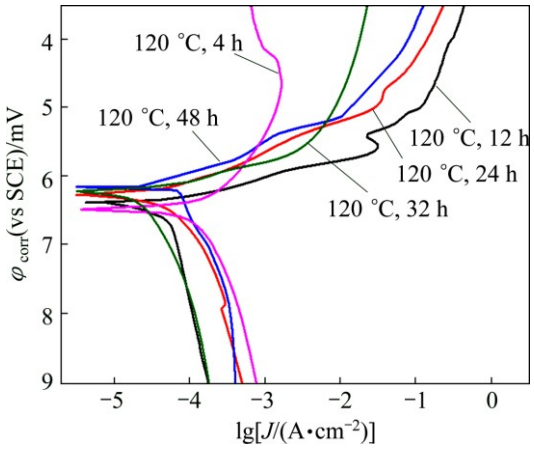

Fig. 10 Polarization curves of studied alloy under various aging conditions

Table 4 Electrochemical parameters of specimens in EXCO solution attainted from polarization test

Aging treatment	φ_{corr}/mV	J_{corr}/(μA·cm^{-2})	R_p/(Ω·cm^{-2})
120 °C, 4 h	−0.648	178.1	47.3
120 °C, 12 h	−0.636	164.3	56.4
120 °C, 24 h	−0.625	127.5	75.8
120 °C, 32 h	−0.619	120.6	79.4
120 °C, 48 h	−0.614	118.5	82.5

3.3.4 EIS analysis

Figure 11 shows Nyquist plots of the studied alloy. At the initial immersion process, there are a capacitive impedance loop in the high-medium frequency region and an inductive impedance loop in the low frequency region (immersion time of 6 and 18 h). The high-medium

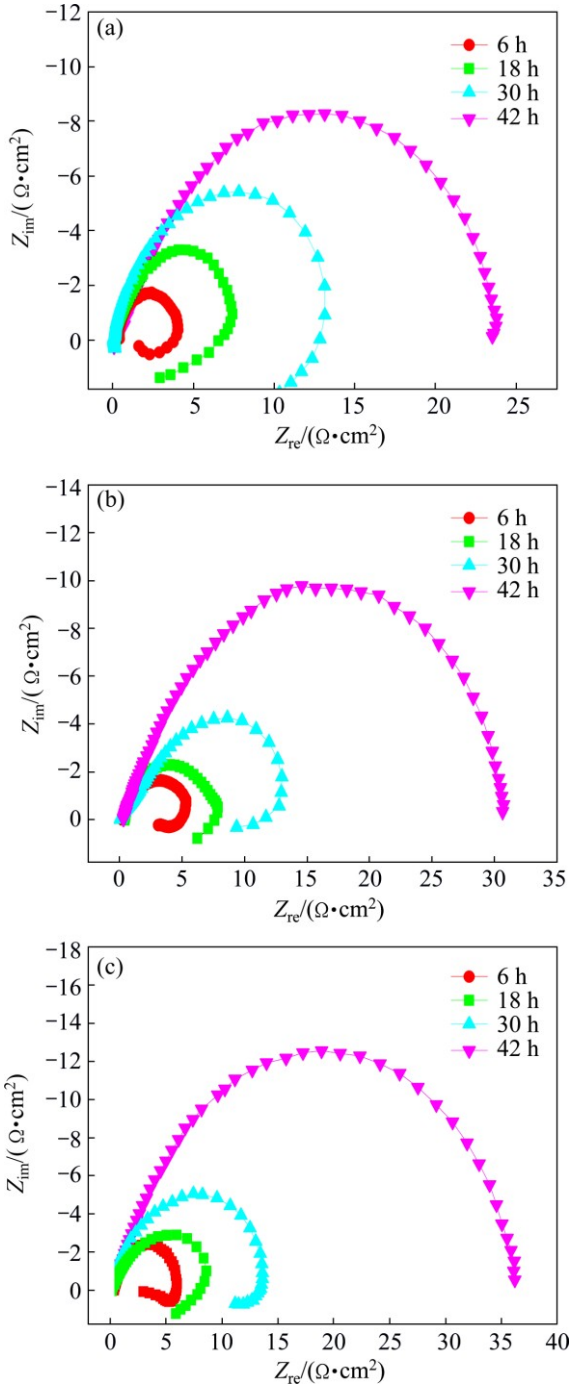

Fig. 11 Nyquist plots of studied alloy immersed in EXCO solution after aged at 120 °C for various time: (a) 4 h; (b) 12 h; (c) 32 h

frequency capacitive loop is attributed to the charge transfer reaction in the electric double layer formed at the interface between metal surface and corrosive solution, and the low frequency inductance loop is attributed to the initiation of corrosion [9]. With increasing immersion time, the surface oxide layer becomes progressively less and less protective, due to the action of aggressive anions of EXCO solution, and the bare new metal is attacked. Then, the relaxation of weak points becomes vanishingly

small. When the immersion time is less than 30 h, inductive loops in the low frequency region are observed from Figs. 11(a), (b) and (c). However, the inductive loops of the studied alloy vanish with increasing immersion time (more than 30 h). In addition, the diameters of the curves of the studied alloy increase with increasing immersion time.

Figure 12 shows the evolution of Bode plots of the studied alloy. It can be easily found from Fig. 12 that there is only one time constant at the initial stage of immersion (less than 30 h). In general, the time constant is related to the attack which is localized on small pits distributed through the surface; the attack extends beneath the alloy surface and forms paths which connect the inner metal surface with the aggressive medium, and there is hardly any detachment of the surface grains. The impedance response mainly proceeds from the flat part on the working electrode [39]. With increasing immersion time (more than 30 h), two time constants can be easily found in Figs. 12(a) and (b). This is because the bare metal is attacked, the corrosion solution gets to the interface of the substrate, and a corrosion micro-battery is formed at the interface. XIAO et al [10] presented that the more clearly the two time constants can be distinguished, the greater the delamination becomes.

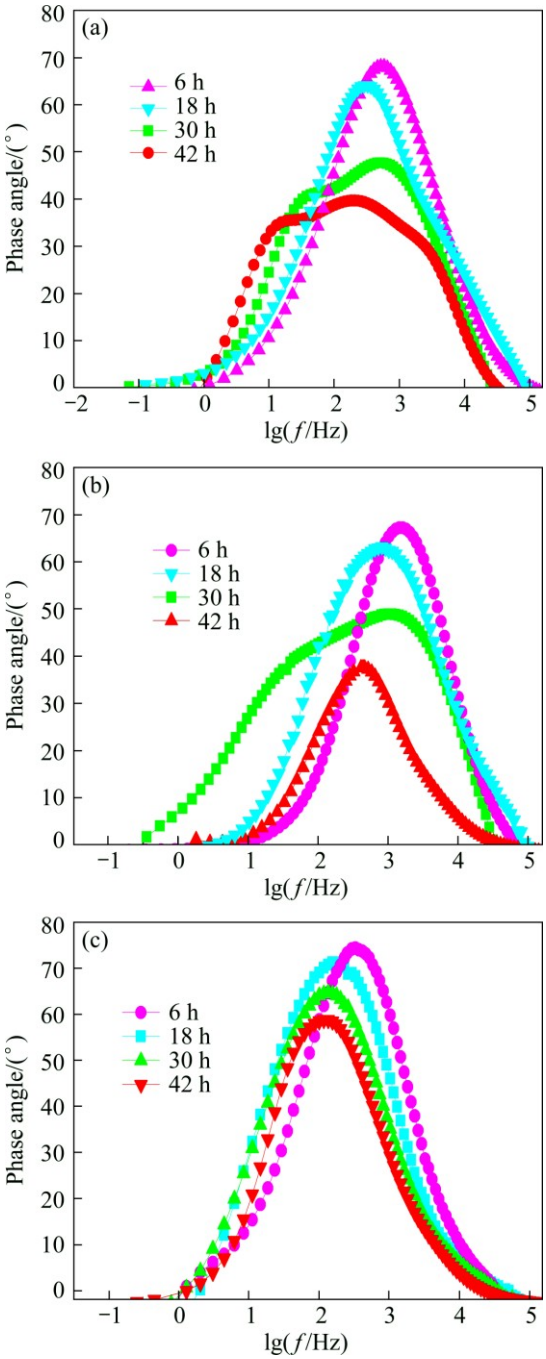

Fig. 12 Bode plots of studied alloy immersed in EXCO solution after aged 120 °C for various time: (a) 4 h; (b) 12 h; (c) 32 h

Figure 13 shows the equivalent circuit used to fit the behavior of the studied alloy immersed in EXCO solution. The physical significance of these elements can be described as follows: R_{sol} corresponds to solution resistance; C_1 presents the capacitance of the film; R_{po} presents the pore resistance of the film; C_2 presents the capacitance of the double layer of the aluminum alloy; and R_{ct} presents the polarization resistance of the electrode. In this circuit, capacitance was mathematically modeled using constant phase element (CPE) in order to obtain a better simulation between the model and the experimental data [40]. Then, the impedance was defined by

$$Z_{CPE} = \frac{Z_0}{(jw)^n} \tag{1}$$

where n can range from −1 to 1, and Z_0 is a constant. For n=1, Z_{CPE} represents an ideal capacitance; n=0, a resistance; n=−1, an inductance; and n=0.5, a Warburg impedance. The EIS data were analyzed in terms of an appropriate equivalent circuit using the ZSimpWin software, and the values of the parameters were determined by the simulation.

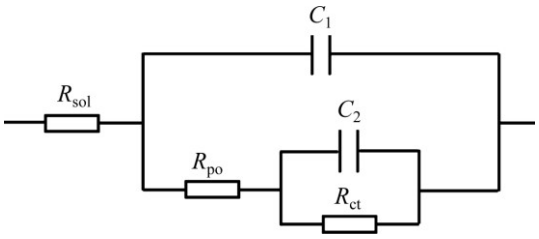

Fig. 13 Equivalent circuit used to fit behavior of studied alloy immersed in EXCO solution

Figure 14 illustrates Nyquist plots and Bode plots of the studied alloy aged at 120 °C for 48 h. It is possible to see the fact that the simulated data have a good agreement with the experimental ones. Tables 5−8 list the fitted circuit constants. Compared with the resistances of R_{po} and R_{ct}, R_{sol} can be ignored. The values of R_{po} and R_{ct} remarkably influence the values

of impedance. Under the same aging treatment, R_{ct} decreases with increasing immersion time (Tables 5−8). With increasing aging time, R_{ct} value increases at the same immersion time, which indicates that the corrosion resistance of the studied alloy can be enhanced with increasing aging time.

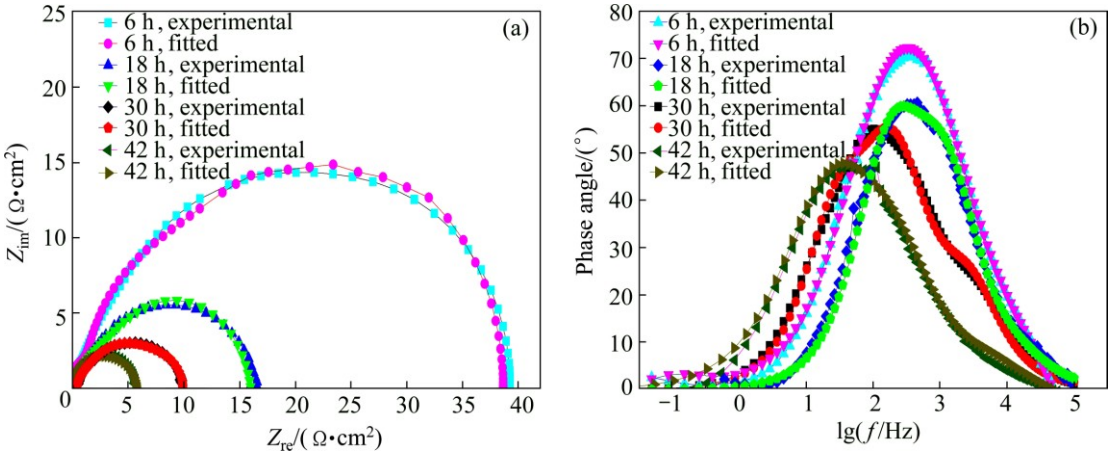

Fig. 14 Nyquist (a) and Bode (b) plots of studied alloy aged at 120 °C for 48 h consisting of experimental and fitted data

Table 5 Electrochemical parameters obtained by fitting analysis of impedance of studied alloy aged at 120 °C for 4 h

Immersion time/h	R_{sol}/(Ω·cm^{-2})	R_{po}/(Ω·cm^{-2})	CPE$_1$		R_{ct}/(Ω·cm^{-2})	CPE$_2$	
			C_1/(F·cm^{-2})	n_1		C_2/(F·cm^{-2})	n_2
6	1.75	35.18	4.12×10^{-5}	0.9745	205.32	5.23×10^{-5}	0.9284
18	1.89	38.02	4.97×10^{-5}	0.9234	88.51	4.53×10^{-5}	0.9648
30	2.12	39.98	5.66×10^{-5}	0.8956	52.35	3.97×10^{-5}	0.9057
42	1.93	42.56	6.54×10^{-5}	0.9315	39.18	3.21×10^{-5}	0.8501

Table 6 Electrochemical parameters obtained by fitting analysis of impedance of studied alloy aged at 120 °C for 12 h

Immersion time/h	R_{sol}/(Ω·cm^{-2})	R_{po}/(Ω·cm^{-2})	CPE$_1$		R_{ct}/(Ω·cm^{-2})	CPE$_2$	
			C_1/(F·cm^{-2})	n_1		C_2/(F·cm^{-2})	n_2
6	1.84	32.45	3.86×10^{-5}	0.9653	217.56	6.01×10^{-5}	0.9336
18	1.56	35.76	4.57×10^{-5}	0.9518	102.35	5.45×10^{-5}	0.8854
30	2.31	38.92	5.43×10^{-5}	0.9845	80.24	4.82×10^{-5}	0.9716
42	2.14	40.16	6.01×10^{-5}	0.8978	42.38	4.23×10^{-5}	0.9274

Table 7 Electrochemical parameters obtained by fitting analysis of impedance of studied alloy aged at 120 °C for 32 h

Immersion time/h	R_{sol}/(Ω·cm^{-2})	R_{po}/(Ω·cm^{-2})	CPE$_1$		R_{ct}/(Ω·cm^{-2})	CPE$_2$	
			C_1/(F·cm^{-2})	n_1		C_2/(F·cm^{-2})	n_2
6	2.15	27.32	3.25×10^{-5}	0.9312	232.95	6.88×10^{-5}	0.8845
18	1.76	29.51	3.67×10^{-5}	0.9487	128.72	6.02×10^{-5}	0.8913
30	1.94	32.08	4.02×10^{-5}	0.9526	65.49	5.56×10^{-5}	0.9514
42	1.53	35.19	4.51×10^{-5}	0.9812	58.26	4.91×10^{-5}	0.9642

Table 8 Electrochemical parameters obtained by fitting analysis of impedance of studied alloy aged at 120 °C for 48 h

Immersion time/h	R_{sol}/(Ω·cm^{-2})	R_{po}/(Ω·cm^{-2})	CPE$_1$		R_{ct}/(Ω·cm^{-2})	CPE$_2$	
			C_1/(F·cm^{-2})	n_1		C_2/(F·cm^{-2})	n_2
6	2.75	18.41	2.54×10^{-5}	0.9745	254.61	7.56×10^{-5}	0.9965
18	1.83	20.16	3.03×10^{-5}	0.9637	136.27	6.88×10^{-5}	0.9517
30	2.21	24.42	3.42×10^{-5}	0.8948	59.35	6.31×10^{-5}	0.8921
42	1.65	28.75	4.11×10^{-5}	0.9213	71.39	5.67×10^{-5}	0.8849

4 Conclusions

1) The ingots of Al−Zn−Mg alloy exhibit serious segregation phenomenon. A large number of Zn- and Mg-enriched non-equilibrium phases are dissolved into α(Al) matrix by homogenization treatment at 470 °C for 24 h. After hot and cold rolling, the grains structures present typical fibrous structures along rolling direction.

2) The ultimate tensile strength and yield strength values of the studied alloy increase firstly and then decrease slightly with increasing aging time. The ultimate tensile strength and yield strength of the studied alloy aged at 120 °C for 24 h can reach maximum values, 584 and 561 MPa, respectively. The hardness of the studied alloy aged at 120 °C for 24 h is about HV 188.4, much higher than that of the alloy aged at 120 °C for 48 h.

3) With increasing aging time, the grain boundary precipitates become coarser, which are distributed along grain boundaries discontinuously. The distributed spacing of grain boundary precipitates becomes larger, and also the width of the PFZ becomes larger.

4) Increasing aging time can effectively enhance the corrosion resistance to IGC and EXCO, due to the coarsening and discontinuous grain boundary precipitates, the increased width of PFZ and the electrochemical behavior of α(Al) matrix, PFZ and grain boundary precipitates.

References

[1] WILLIAMS J C, STRAKE E A. Process in structural materials for aerospace systems [J]. Acta Materialia, 2003, 51: 5775−5799.

[2] ZAINUL H, PRASETYO E. Materials selection in design of structures and engines of supersonic aircrafts: A review [J]. Materials and Design, 2013, 46: 552−560.

[3] NIE Xiao-wu, ZHANG Li-jun, DU Yong. Experiments and modeling of double-peak precipitation hardening and strengthening mechanisms in Al−Zn−Mg alloy [J]. Transactions of Nonferrous Metals Society of China, 2014, 24: 2138−2144.

[4] ZHOU Kun, WANG Bin, ZHAO Yu, LIU Jie. Corrosion and electrochemical behaviors of 7A09 Al−Zn−Mg−Cu alloy in chloride aqueous solution [J]. Transactions of Nonferrous Metals Society of China, 2015, 25: 2509−2515.

[5] FANG Hua-chan, CHAO Hua, CHEN Kang-hua. Effect of Zr, Er and Cr additions on microstructures and properties of Al−Zn−Mg−Cu alloys [J]. Materials Science and Engineering A, 2014, 610: 10−16.

[6] ZHANG Yong-zhi, GU Jing, TIAN Yuan, GAO Hai-yan, WANG Jun, SUN Bao-de. Microstructural evolution and mechanical property of Al−Zr and Al−Zr−Y alloys [J]. Materials Science and Engineering A, 2014, 616: 132−140.

[7] WU H, WEN S P, GAO K Y, HUANG H, WANG W, NIE Z R. Effect of Er additions on the precipitation strengthening of Al−Hf alloys [J]. Scripta Materialia, 2014, 87: 5−8.

[8] VO N Q, DUNAND D C, SEIDMAN D N. Improving aging and creep resistance in a dilute Al−Sc alloy by microalloying with Si, Zr and Er [J]. Acta Materialia, 2014, 63: 73−85.

[9] DENG Ying, XU Guo-fu, YIN Zhi-min, LEI Xue-feng, HUANG Ji-wu. Effects of Sc and Zr microalloying additions on the recrystallization texture and mechanism of Al−Zn−Mg alloys [J]. Journal of Alloys and Compounds, 2013, 580: 412−426.

[10] XIAO Yan-ping, PAN Qing-lin, LI Wen-bin, LIU Xiao-yan, HE Yun-bin. Influence of retrogression and reaging treatment on corrosion behaviour of an Al−Zn−Mg−Cu alloy [J]. Materials and Design, 2011, 32: 2149−2156.

[11] LIU Xiao-yan, LI Meng-jie, GAO Fei, LIANG Shun-xing, ZHANG Xi-liang, CUI Hao-xuan. Effects of aging treatment on the intergranular corrosion behavior of Al−Cu−Mg−Ag [J]. Journal of Alloys and Compounds, 2015, 639: 263−267.

[12] WANG X H, WANG J H, YUE X, GAO Y. Effect of aging treatment on the exfoliation corrosion and stress corrosion cracking behaviors of 2195 Al−Li alloy [J]. Materials and Design, 2015, 67: 596−605.

[13] WANG S D, XU D K, CHEN X B, HAN E H, DONG C. Effect of heat treatment on the corrosion resistance and mechanical properties of an as-forged Mg−Zn−Y−Zr alloy [J]. Corrosion Science, 2015, 92: 228−236.

[14] ROGAL Ł, DUTKIEWICZ J, SZKLARZ Z, KRAWIEC H, KOT M, ZIMOWSKI S. Mechanical properties and corrosion resistance of steel X210CrW12 after semi-solid processing and heat treatment [J]. Materials Characterization, 2014, 88: 100−110.

[15] LI H Y, KANG W, LU X C. Effect of age-forming on microstructure, mechanical and corrosion properties of a novel Al−Li alloy [J]. Journal of Alloys and Compounds, 2015, 640: 210−218.

[16] WANG Z X, LI H, MIAO F F, SUN W J, FANG B J, SONG R G, ZHENG Z Q. Improving the intergranular corrosion resistance of Al−Mg−Si−Cu alloys without strength loss by a two-step aging treatment [J]. Materials Science and Engineering A, 2014, 590: 267−273.

[17] GB/T 22639−2008. Test method of exfoliation corrosion for wrought aluminum and aluminum alloys [S].

[18] GB/T 7998−2005. Test method for inter-granular corrosion of aluminum alloys [S].

[19] LI Bo, PAN Qing-lin, SHI Yun-jia, LI Chen, YIN Zhi-min. Microstructural evolution of Al−Zn−Mg−Zr alloy with trace amount of Sc during homogenization treatment [J]. Transactions of Nonferrous Metals Society of China, 2013, 23: 3568−3574.

[20] WU L M, WANG W H, HSU Y F, TRONG S. Effects of homogenization treatment on recrystallization behavior and dispersoid distribution in an Al−Zn−Mg−Sc−Zr alloy [J]. Journal of Alloys and Compounds, 2008, 456: 163−169.

[21] AIURA T, SUGAWARA N, MIURA Y. The effect of scandium on the as-homogenized microstructure of 5083 alloy for extrusion [J]. Materials Science and Engineering A, 2000, 280:139−145.

[22] JONES M J, HUMPHREYS F J. Interaction of recrystallization and precipitation: the effect of Al_3Sc on the recrystallization behaviour of deformed aluminium [J]. Acta Materialia, 2003, 51: 2149−2159.

[23] SENKOV O N, SHAGIEV M R, SENKOVA S V, MIRACLE D B. Precipitation of Al_3(Sc,Zr) particles in an Al−Zn−Mg−Cu−Sc−Zr alloy during conventional solution heat treatment and its effect on tensile properties [J]. Acta Materialia, 2008, 56: 3723−3738.

[24] ZANDER D, SCHNATTERER C, ALTENBACH C, CHAINEUX V. Microstructural impact on intergranular corrosion and the mechanical properties of industrial drawn 6056 aluminum wires [J]. Materials and Design, 2015, 83: 49−59.

[25] CHEN B A, PAN L, WANG R H, LIU G, CHENG P M, XIAO L, SUN J. Effect of solution treatment on precipitation behaviors and age hardening response of Al−Cu alloys with Sc addition [J]. Materials Science and Engineering A, 2011, 530: 607−617.

[26] LIN Y C, ZHANG J L, LIU G, LIANG Y J. Effects of pre-treatments on aging precipitates and corrosion resistance of a creep-aged Al−Zn−Mg−Cu alloy [J]. Materials and Design, 2015, 83: 866−875.

[27] GOPALA KRISHNA K, SIVAPRASAD K, VENKATESWARLU K, HARI KUMAR K C. Microstructural evolution and aging behavior of cryorolled Al−4Zn−2Mg alloy [J]. Materials Science and Engineering A, 2012, 535: 129−135.
[28] WU L M, SEYRING M, RETTENMAYR M, WANG W H. Characterization of precipitate evolution in an artificially aged Al−Zn−Mg−Sc−Zr alloy [J]. Materials Science and Engineering A, 2010, 527: 1068−1073.
[29] YANG W C, JI S X, ZHANG Q, WANG M P. Investigation of mechanical and corrosion properties of an Al−Zn−Mg−Cu alloy under various ageing conditions and interface analysis of η' precipitate [J]. Materials and Design, 2015, 85: 752−761.
[30] MARLAUD T, MALKI B, HENON C, DESCHAMPS A, BAROU B. Relationship between alloy composition, microstructure and exfoliation corrosion in Al−Zn−Mg−Cu alloys [J]. Corrosion Science, 2011, 53(10): 3139−3149.
[31] FANG H C, CHAO H, CHEN K H. Effect of recrystallization on intergranular fracture and corrosion of Al−Zn−Mg−Cu−Zr alloy [J]. Journal of Alloys and Compounds, 2015, 622: 166−173.
[32] KNIGHT S P, BIRBILIS N, MUDDLE B C, TRUEMAN A R, LYNCH S P. Correlations between intergranular stress corrosion cracking, grain-boundary microchemistry, and grain-boundary electrochemistry for Al−Zn−Mg−Cu alloys [J]. Corrosion Science, 2010, 52(12): 4073−4080.
[33] LIN Y C, JIANG Y Q, ZHANG X C, DENG J, CHEN X M. Effect of creep-aging processing on corrosion resistance of an Al−Zn−Mg−Cu alloy [J]. Materials and Design, 2014, 61: 228−238.
[34] WLOKA J, HACK T, VIRTANEN S. Influence of temper and surface condition on the exfoliation behaviour of high strength Al−Zn−Mg−Cu alloys [J]. Corrosion Science, 2007, 49(3): 1437−1449.
[35] CAVANAUGH M K, BIRBILISA N, BUCHHEITA R G, BOVARD F. Investigating localized corrosion susceptibility arising from Sc containing intermetallic Al_3Sc in high strength Al-alloys [J]. Scripta Materialia, 2007, 56: 995−998.
[36] SHI Yun-jia, PAN Qing-lin, LI Meng-jia, HUANG Xing, LI Bo. Effect of Sc and Zr additions on corrosion behaviour of Al−Zn−Mg−Cu alloys [J]. Journal of Alloys and Compounds, 2014, 612: 42−50.
[37] KANNAN M B, RAJA V S. Influence of heat treatment and scandium addition on the electrochemical polarization behavior of Al−Zn−Mg−Cu−Zr (7010) alloy [J]. Metallurgical and Materials Transactions A, 2007, 38: 2843−2852.
[38] CHEN K H, FANG H C, ZHANG Z, CHEN X, LIU G. Effect of of Yb, Cr and Zr additions on recrystallization and corrosion resistance of Al−Zn−Mg−Cu alloys[J]. Materials Science and Engineering A, 2008, 497: 426−431.
[39] DENG Ying, YIN Zhi-min, ZHAO Kai, DUAN Jia-qi, HU Jian, HE Zhen-bo. Effects of Sc and Zr microalloying additions and aging time at 120 °C on the corrosion behaviour of an Al−Zn−Mg alloy [J]. Corrosion Science, 2012, 65: 288−298.
[40] CONDE A, DAMBORENEA J D. Evaluation of exfoliation susceptibility by means of the electrochemical impedance spectroscopy [J]. Corrosion Science, 2000, 42: 1363−1377.

时效时间对一种新型 Al−Zn−Mg−Sc−Zr 合金析出行为、力学和腐蚀性能的影响

李 波[1]，潘清林[2]，陈从平[1]，尹志民[2]

1. 三峡大学 机械与动力学院，宜昌 443002；
2. 中南大学 材料科学与工程学院，长沙 410083

摘 要：通过光学显微镜、扫描电镜、透射电镜、拉伸实验、极化曲线和电化学阻抗谱等方法研究时效时间对一种新型 Al−Zn−Mg−Sc−Zr 合金析出行为、力学和腐蚀性能的影响。结果表明：当合金经过 120 °C 时效时，随着时效时间的延长，合金的硬度和拉伸强度呈先快速增加后逐渐降低的趋势。同时，合金的抗剥落腐蚀和晶间腐蚀性能随着时效时间的延长逐渐提高，与极化曲线和电化学阻抗谱呈现的趋势保持一致。合金的晶界析出行为和无沉淀析出带对其力学和腐蚀行为有着重要的影响。由透射电镜观察到的组织可知，随着时效时间的延长，晶界析出相逐渐粗化，无沉淀析出带变宽，且晶界析出相间距变大。

关键词：铝合金；热处理；析出行为；$Al_3(Sc, Zr)$粒子；电化学阻抗谱

(Edited by Wei-ping CHEN)